

Temperature-induced band renormalization and Lifshitz transition in a kagome superconductor RbV_3Sb_5

Zhonghao Liu,^{1,2,*} Ningning Zhao,³ Qiangwei Yin,³ Chunsheng Gong,³ Zhijun Tu,³ Man Li,³ Wenhua Song,³ Zhengtai Liu,¹ Dawei Shen,^{1,2} Yaobo Huang,⁴ Kai Liu,^{3,†} Hechang Lei,^{3,‡} and Shancai Wang^{3,§}

¹*State Key Laboratory of Functional Materials for Informatics,
Shanghai Institute of Microsystem and Information Technology,
Chinese Academy of Sciences, Shanghai 200050, China*

²*College of Materials Science and Opto-Electronic Technology,
University of Chinese Academy of Sciences, Beijing 100049, China*

³*Department of Physics and Beijing Key Laboratory of Opto-Electronic Functional
Materials&Micro-Nano Devices, Renmin University of China, Beijing 100872, China*

⁴*Shanghai Advanced Research Institute, Chinese Academy of Sciences, Shanghai 201204, China*

Recently discovered Z_2 topological kagome metals $AV_3\text{Sb}_5$ ($A = \text{K, Rb, and Cs}$) exhibit intriguing transport anomalies and novel superconducting paring states, providing a versatile platform for studying interplay between electron correlation and quantum orders. Here we directly visualise how temperature drives band renormalization and Lifshitz transition in RbV_3Sb_5 using angle-resolved photoemission spectroscopy, pointing to the key role of tuning van Hove singularities to the Fermi energy in mechanisms of both CDW and superconducting orders. Multiple singularities with different energies and orbital characters could induce various ordering phases, including superconductivity if cooperating with matching bosons. Considering the existence of the non-trivial topological Dirac surface states at the time-reversal-invariant momentum points, they may also provide a promising route to realize zero energy modes related to Majorana fermions. Our findings are significant in understanding abundant transport behaviors and quantum phases in these kagome superconductors.

Layered kagome-lattice transition metals are emerging as an exciting platform to explore the frustrated lattice geometry and quantum topology. A typical kagome-lattice electronic band produced by the tight-binding model is characterized by a Dirac dispersion at the Brillouin zone (BZ) corner, a saddle point at the zone boundary, and a flat band through the BZ. The versatile quantum phenomena can be realized by tuning any of them close to the Fermi energy (E_F), such as Dirac/Weyl fermions [1–13], ferromagnetism [14–16], negative flat band magnetism [17], and topological Chern magnet [18]. Recently, superconductivity is discovered in a new family of layered kagome metals $AV_3\text{Sb}_5$ ($A = \text{K, Rb, and Cs}$) ($T_c \sim 0.9\text{--}2.5$ K) [19–23], which host a Z_2 topological invariant and non-trivial topological Dirac surface states near E_F [20]. These materials exhibit transport and magnetic anomalies about 80–100 K [19–23], which are evidenced to be due to competing electronic orders at the saddle-point singularity with high density of states [24–36]. X-ray diffraction and scanning tunneling microscopy reveal the formation of a three-dimensional (3D) $2 \times 2 \times 2$ superlattice at both charge density wave (CDW) and superconducting states [23–27], which energetically favors a chiral charge order and an inverse Star of David distortion in kagome lattice with the shift of van Hove singularity to E_F [33, 34, 37]. A giant anomalous Hall effect with the reversal of Hall sign at about 50 K is observed at low temperature [21], while magnetic order and local moments are not found by magnetic susceptibility and muon spin spectroscopy [21, 22, 38]. In addition, the observed dou-

ble superconducting domes and exotic pairing states are associated with the singularities near E_F [26–36, 39–42], which at present need to be further studied in details. To fundamentally understand these anomalies behaviors and quantum orders, the investigation of temperature evolution of the low-energy electronic structure is highly desired.

In this paper, we present the temperature evolution of the bands near E_F in Z_2 topological metal RbV_3Sb_5 by utilizing angle-resolved photoemission spectroscopy (ARPES). We found that the holelike band at the BZ center ($\bar{\Gamma}$) is shifted up about 0.13 eV from ~ 120 K to 10 K and the electronlike bands at the zone boundary (\bar{M}) with their bottoms approaching E_F is shifted down about 0.04 eV from ~ 120 to 90 K, which reveals electronic correlation being enhanced due to the formation of charge orders. One of the bands centred at the \bar{M} points continues to be flatten below ~ 90 K and sunk below E_F around 70 K causing the Lifshitz transition, which could induce the reversal of Hall sign due to increasing electron occupation. The existence of the Dirac surface states at the time-reversal-invariant \bar{M} points may provide a promising route to realize zero energy modes related to Majorana fermions. The temperature-induced bands renormalization and Lifshitz transition can account for anomalies transport behaviors, strongly implying that they are the multiple singularities which play ultimate roles in mechanisms of both CDW and superconducting phases.

The crystal structure of RbV_3Sb_5 crystallizes in a hexagonal structure with $P6/mmm$ (No. 191) space group [19–23], in which V-Sb slabs consisting of V kagome nets and interspersing Sb atoms are separated by alkali metal ions along c axis, as shown in Fig. 1a. There are two kinds of Sb sites: Sb1 site at the centers of V hexagons, and Sb2 site below and above the centers of V triangles forming hexagon layers. The corresponding original (red lines) and 2×2 reconstructed

* lzh17@mail.sim.ac.cn

† kliu@ruc.edu.cn

‡ hlei@ruc.edu.cn

§ scw@ruc.edu.cn

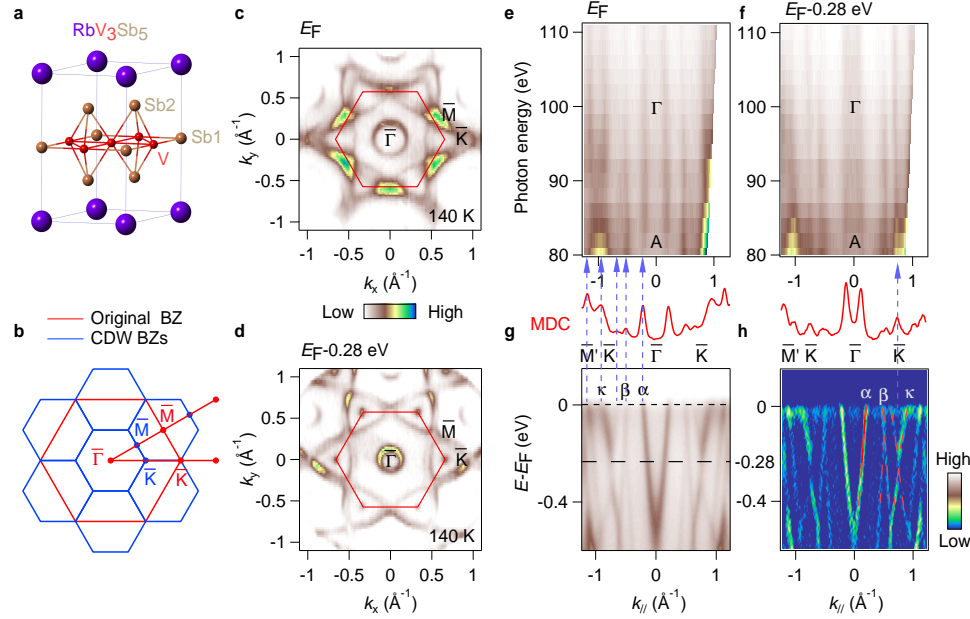


FIG. 1. 2D Fermi surfaces and Dirac bands. **a** Crystal structure of RbV_3Sb_5 with space group $P6/mmm$ (No. 191). **b** The original (red lines) and 2×2 reconstructed (blue lines) BZs projected on the (001) surface with the high-symmetry points. **c, d** Integrated intensity plot (± 10 meV) at E_F and 0.28 eV below E_F taken at 140 K. The red lines indicate the high-symmetry directions and the original BZs. **e, f** Integrated intensity plots (± 10 meV) on the $h\nu$ - k_{\parallel} plane at E_F and 0.28 eV below E_F with k_{\parallel} oriented along the $\bar{\Gamma} - \bar{K}$ direction. The high-symmetry points are plotted. **g, h** Intensity plot and corresponding second derivative plot along the $\bar{\Gamma} - \bar{K}$ direction. The bands are indicated by the Greek letters and the red dashed lines.

(blue lines) BZs projected on the (001) surface with the high-symmetry points are shown in Fig. 1b. Figures 1c, d show constant-energy surfaces at E_F and E_F -0.28 eV, respectively, taken above CDW transition temperature (T_{CDW}). The high intensity around the \bar{M} points at the Fermi surfaces suggests the singularities or the surface states at the proximity of E_F . To investigate the 3D character of the Fermi surfaces, we carried out the photon-energy-dependent ARPES measurement. With an empirical value of the inner potential of ~ 17 eV and $c = 9.07 \text{ \AA}$ [23], we found that $h\nu = 100$ eV is close to the Γ point and 82 eV close to the A point, according to the free-electron final-state model [43]. Three electronlike pockets (α , β , and κ) along the $\bar{\Gamma} - \bar{K}$ direction are indicated in Figs. 1g, h. All of the three bands show weak k_z dispersions both at E_F and E_F -0.28 eV as shown in Figs. 1e, f, which reveal the two-dimensional (2D) Fermi surfaces and 2D Dirac cones at the \bar{K} points. Due to the observed weak k_z dispersions, for conveniently, hereafter we will always use the projected 2D BZ ($\bar{\Gamma} - \bar{K} - \bar{M}$) in below discussion unless otherwise specified. Based on the ARPES data, we estimate that the widths of the α , β , and κ Fermi pockets along $\bar{\Gamma} - \bar{K}$ are about 0.42, 0.10, and 0.31 \AA^{-1} and the Fermi velocities of them are about 3.25, 3.60, and 1.70 eV \AA (1.28 eV \AA for another branch of Dirac bands), respectively. It is noticeable that the β band with its bottom at about 0.07 eV below E_F could induce the quantum oscillation [22].

Figure 2 shows the bands along the $\bar{\Gamma} - \bar{M}$ direction taken at different temperatures. The half strong and half weak intensity at \bar{M} in Fig. 2a-d could be induced by matrix element effect on the small tips of the bands top and bottom near M , as shown in the calculated bands of Fig. 4. Figure 2e shows the momentum distribution curves (MDCs) of the α band at $\bar{\Gamma}$ taken at 120 K, revealing the two splitting sub-branches. The STM results suggest an isotropic scattering vector connecting different states of the α pocket [25–27], but the two Sb sites or k_z integration can also cause the bands splitting in the ARPES experiments. By comparing the data taken at different temperatures, one can clearly see that the α band bottom is shifted up about 0.13 eV from 120 K to 10 K as shown in the plot of the energy distribution curves (EDCs) at the $\bar{\Gamma}$ center (Fig. 2f), and the Fermi crossing is not evident to be changed below 100 K (Fig. 2g). Thus the α band is largely condensed rather than the entirely rigid shifting up. Comparing with the calculated bandwidth of the α band (~ 0.74 eV) (Fig. 4a), the α band along the $\bar{\Gamma} - \bar{M}$ direction needs to be renormalized by a factor of about 1.3 below 10 K. At the \bar{M} point, the κ' and γ bands can be observed at 120 K (Fig. 2h). The two bands are shifted down at 10 K and the δ band is brought out (Fig. 2i). The δ band could be an edge state cut by the Fermi distribution function. We display in details the temperature-dependent data in Fig. 2j, from which one can find that the κ' and γ bands begin to be shifted down around T_{CDW} and stand

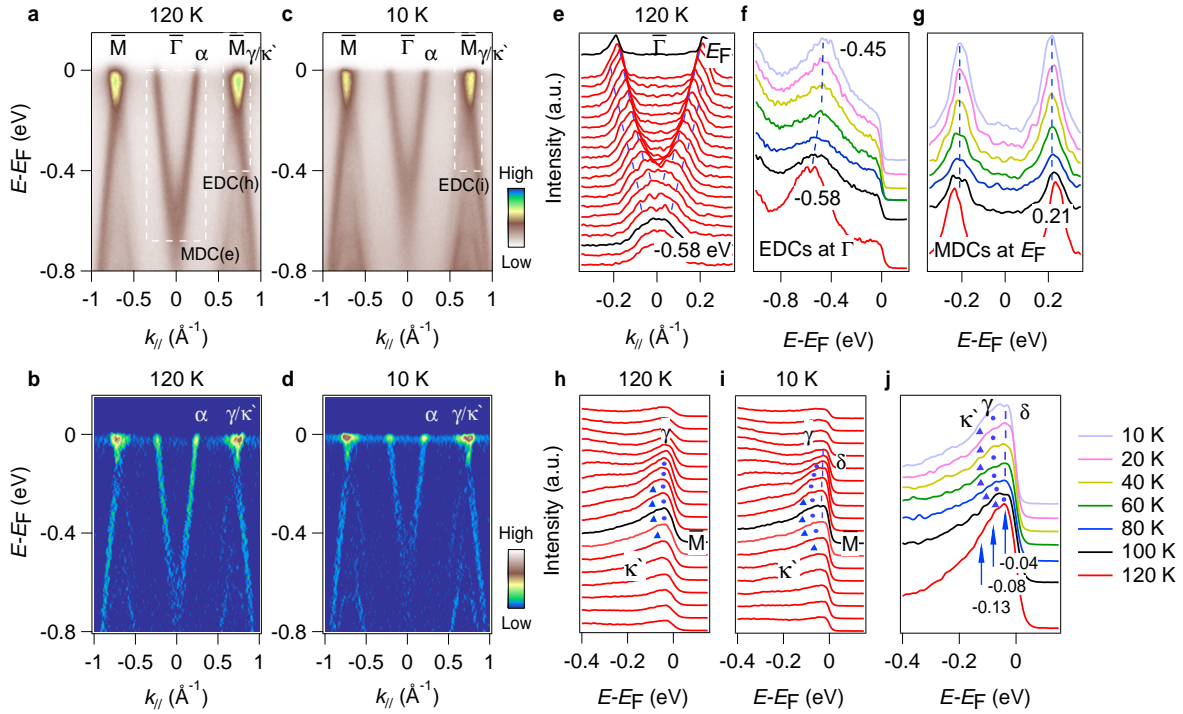


FIG. 2. **Temperature-induced band renormalization along $\bar{\Gamma} - \bar{M}$.** **a, b** Intensity plot and corresponding second derivative plot along the $\bar{\Gamma} - \bar{M}$ direction taken at 120 K. The bands are indicated by the Greek letters. **c, d** The same as **a** and **b**, but taken at 10 K. **e** MDCs around the $\bar{\Gamma}$ point taken at 140 K, as indicated by the dashed rectangles in **a**. **f** EDCs at the $\bar{\Gamma}$ center taken at different temperatures. **e** MDCs at E_F taken at different temperatures. **h, i** EDCs around the M point at 120 K and 10 K, as indicated by the dashed rectangles in **a** and **c**. **j** EDCs at the \bar{M} center taken at different temperatures. Different colors represent different temperatures.

steadily around 80 K with the band bottoms at 0.08 and 0.13 eV below E_F , respectively. We estimate that the widths of the α , κ' , and γ Fermi pockets along $\bar{\Gamma} - \bar{M}$ at 10 K are about 0.42, 0.22, and 0.10 \AA^{-1} and the Fermi velocities of them are about 3.32, 1.68, and 4.20 eV \AA , respectively. The γ band could also induce the quantum oscillation [22].

Figure 3 shows the bands along the $\bar{K} - \bar{M}$ direction taken at different temperatures. From intensity plots and the corresponding EDCs (Figs. 3a-g), one can clearly see that the bands near the \bar{M} point are remarkably changed at different temperatures. The κ' band crosses E_F at 140 K as shown in Fig. 3d. The κ' and γ bands shifting down along with decreasing temperature mentioned above can be more clearly identified along the $\bar{K} - \bar{M}$ direction, as shown in Fig. 3h. More strikingly, when the two bands bottoms are not moved around 70-90 K (Fig. 3h), the κ' band centred at \bar{M} continues to be flatten below ~ 90 K and sunk below E_F at ~ 70 K causing the Lifshitz transition, which could induce the reversal of Hall sign due to increasing electron occupation. At 30 K, the tip of the κ' band is located about 0.04 eV below E_F . The sketch of temperature evolution of the bands near \bar{M} is shown on the left panel of Fig. 3d. In addition, we show the temperature evolution of the Dirac bands at the \bar{K} point in Fig. 3i. The Dirac bands are not visibly moved at different temperatures both along $\bar{K} - \bar{M}$ and $\bar{\Gamma} - \bar{K}$ (not shown here). Therefore, we determine that the moving in the opposite direction of the bands at $\bar{\Gamma}$ and \bar{M} should be associated with the change of in-

trinsic bulk states, rather than a trivial surface reconstruction.

Comparing with the calculated bands along the high-symmetry lines in Fig. 4a, our ARPES data at the \bar{M} point have the calculated features both on $k_z \sim 0$ (M) and $k_z \sim \pi$ (L) planes, as indicated by the red squares. Usually, the k_z integration and matrix element effects in the ARPES spectra reflect that the electronic states are integrated over a certain k_z region of the bulk BZ and the states at $k_z = 0$ and π contribute greatly [44]. In this 3D $2 \times 2 \times 2$ CDW material, the CDW folding bands would also cause and strengthen the folding from $k_z \sim \pi$ to $k_z \sim 0$. In fact, ARPES data taken with various photon energies is more like the calculation of the surface states, as shown in Figs. 4b, c. As a Z_2 topological kagome metal, RbV_3Sb_5 hosts non-trivial topological Dirac surface states at the time-reversal-invariant \bar{M} points and remains the same after the CDW transition. Along $\bar{K} - \bar{M}$, the Dirac surface states with the bands bottom at about 0.04 eV below E_F can be clearly distinguished. Along $\bar{\Gamma} - \bar{M}$, the surface states can also be identified and somehow mixed with the bulk bands. The observed bands at \bar{M} presumably contain the component of the surface states, and the surface bands can also be gapped at E_F by the enhanced CDW orders along with decreasing temperature. Because several bands are squeezed at a small energy and momentum spaces and cut off by the Fermi distribution function, the chemical potential needs to be further much elevated for further studying on the surface states in details. It is possible to realize Majorana zero energy modes and its related

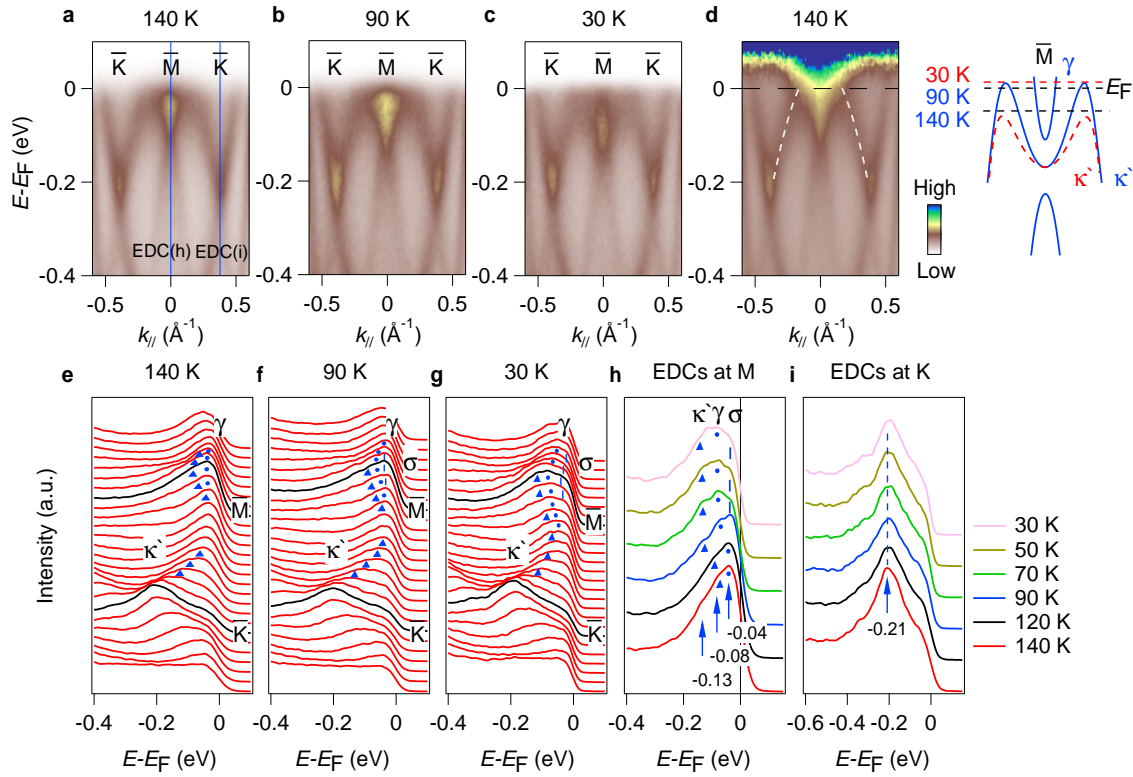


FIG. 3. **Temperature-induced band renormalization and Lifshitz transition along $\bar{K} - \bar{M}$.** **a-c** Intensity plot along the $\bar{K} - \bar{M}$ direction taken at 140, 90 and 30 K, respectively. **d** Intensity plot taken at 140 K. The Fermi distribution function is divided out to reveal features above E_F . The right panel: The sketch of temperature evolution of the bands near \bar{M} . **e-g** EDCs along $\bar{K} - \bar{M}$ corresponds to **a-c**. The bands are indicated by the different symbols. **h** EDCs at the \bar{M} center as indicated by the line in **a**, taken at different temperatures. **i** EDCs at the \bar{K} center as indicated by the line in **a**, taken at different temperatures. Different colors represent different temperatures.

topological superconductivity in these materials.

With the help of the orbital-projection band calculation (Fig. 4a), one can find that the strongly renormalized α band above the Lifshitz transition temperature are mainly contributed by out-of-plane Sb1- p_z (dark). The bondings of the out-of-plane orbitals and the interlayer coupling strengths are being enhanced along with decreasing temperature, which are also revealed by the reduction of the lattice constants of c [20]. The renormalization of the bands of out-of-plane should be more appreciated at the CDW instability and its associated the superconducting states. The 2D Dirac bands at \bar{K} (κ and κ') originate from in-plane V- d_{x2-y2} (carmine red) and V- d_{xy} (red) orbitals, and they are hybridized with V- d_{xz}/d_{yz} (blue) orbitals near the \bar{M} point along $\bar{K} - \bar{M}$. The Lifshitz transition takes place when the tip of this hybridized band is sunk below E_F . Evidently, besides the bands of out-of-plane orbitals, the upper branches of the Dirac bands of in-plane orbitals along $\bar{K} - \bar{M}$ are also strongly renormalized, revealing orbital-selective singularities and their associated ordering phases. Recently the observation of pressure-induced reentrant superconductivity indicates the α band at $\bar{\Gamma}$ and the κ' and γ bands at \bar{M} are further moved in the opposite direction, inducing another Lifshitz transition when the α band bottom emerging above E_F at $\bar{\Gamma}$ [42].

The temperature-induced band renormalization and Lifshitz transition, which are endowed with electronic correlation effect, have a close relationship with CDW and superconducting orders. Actually, the Lifshitz transition can be induced by doping, temperature, or pressure in the other unconventional superconductors, such as cuprates [45], iron pnictides [46], Sr_2RuO_4 [47], and transition metal dichalcogenides [48]. Previous studies provide strong evidences that the Lifshitz transition caused by traversing the singularity to E_F is beneficial in the formation of ordering phenomena. For instance, in CDW material TaSe_2 also with 3D $2 \times 2 \times 2$ superstructure, by tuning the energy position of the singularity, the superconducting critical temperature is enhanced by more than an order of magnitude [48]. There are multiple conceivable singularities near the \bar{M} point in RbV_3Sb_5 according to the recent studies. The formation of CDW states is evidenced to be due to the saddle-point singularity below E_F [23–27]. Around 100 K, the bottoms of the κ' and γ bands close to E_F can be treated as singularities. Lifshitz transition, which could cause Hall sign change [21], gives rise to the proximity of the singularity to E_F . Furthermore, on the basis of calculations, the surface bands bottom could contribute the singularities and preserve the possibility of topological superconductivity. The superconductivity could be realized when the optimal positions of

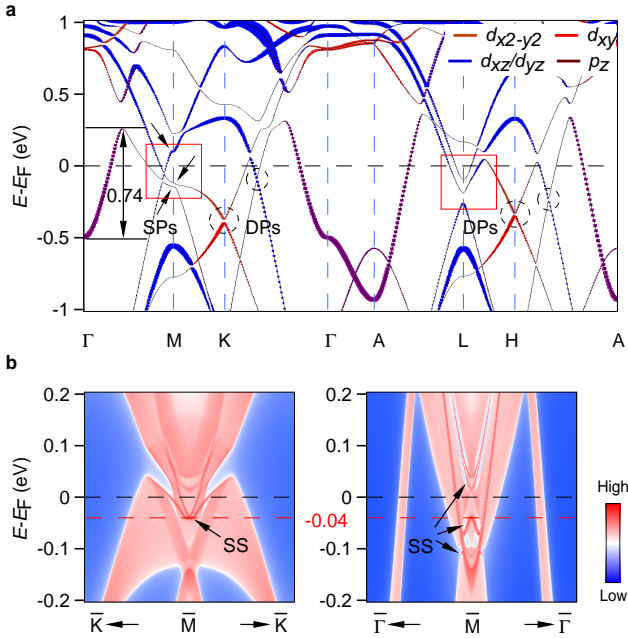


FIG. 4. The calculated bands. **a** Orbital-projection band structure of RbV_3Sb_5 with SOC along the high-symmetry lines. Here the main contribution orbitals near E_F only are shown and the orbital weights are represented by both the colors and the size of the bands. The saddle points (SPs) at M are indicated by the arrows, and the Dirac points (DPs) are marked with the dashed circles. The features at \bar{M} (M and L) are indicated by the red squares. **b** Projected band structures for the (001) surfaces of RbV_3Sb_5 around the \bar{M} point along $\bar{K} - \bar{M}$ and $\bar{\Gamma} - \bar{M}$. The surface states (SSs) are indicated by the arrows.

the singularities with respect to E_F match with the corresponding bosons. Recently, thermal conductivity and high pressure resistance measurements reveal two superconducting domes and exotic pairing states [28, 29, 41, 42], which should be associated with the different energy singularities and paring media. The possibility of magnons is largely ruled out due to the absence of magnetic orders and local moments. The density-wave fluctuation is usually considered as a possible glue in the materials with coexistence of CDW states and superconductivity. Combining our ARPES experiments and recent measurements under high-pressure [42], the strongly renormalized bands near E_F by both temperature and pressure induce the Lifshitz transitions accompanying the rapid change of lattice parameter c , suggesting enhanced electron-phonon coupling due to partial phonon softening.

In summary, we have demonstrated the temperature evolution of the bands E_F in kagome superconductor RbV_3Sb_5 . We observed the temperature-induced band renormalization and Lifshitz transition on the bands with different orbitals characters, which have an intimate relationship with the anomalies transport behaviors and quantum orders. Our findings strongly imply that the orbital-selective singularities near E_F play important roles in mechanisms of ordering phases.

Methods

Experiments details Single crystals of RbV_3Sb_5 were synthesized by the self-flux method as described elsewhere [22]. RbV_3Sb_5 single crystals are stable in the air. ARPES measurements were performed at the Dreamline and 03U beamlines of Shanghai Synchrotron Radiation Facility (SSRF). The energy and angular resolutions were set to better than 24 meV and 0.02 \AA^{-1} , respectively. Samples were cleaved *in situ*, exposing flat mirrorlike (001) surfaces. The pressure was maintained less than 2×10^{-10} Torr during temperature-dependent measurements.

Calculation methods The first-principles electronic structure calculations on RbV_3Sb_5 were performed by using the projector augmented wave (PAW) method [49, 50] as implemented in the Vienna Ab initio Simulation Package (VASP) [51]. The generalized gradient approximation (GGA) of Perdew-Burke-Ernzerhof (PBE) type [52] was used for the exchange-correlation functional. The kinetic energy cutoff of the plane-wave basis was set to be 350 eV. The Brillouin zone was sampled with a $10 \times 10 \times 6$ k -point mesh. For the Fermi surface broadening, the Gaussian smearing method with a width of 0.05 eV was adopted. The zero-damping DFT-D3 method was adopted to describe the interlayer van der Waals (vdW) interactions [53]. The lattice constants and the atomic positions were fully relaxed until the forces on all atoms were smaller than 0.01 eV/ \AA . The relaxed lattice constants $a = b = 5.4333 \text{ \AA}$ and $c = 8.9986 \text{ \AA}$ are consistent with the experiment result [23]. The spin-orbit coupling effect was included in the band structure calculations. The surface states in the projected two-dimensional Brillouin zone were calculated with the surface Green's function method by using the WannierTools package [54]. The tight-binding Hamiltonian of the semi-infinite system was constructed by the maximally localized Wannier functions [55].

Acknowledgements This work was supported by the National Key R&D Program of the Ministry of Science and Technology of China (MOST) (Grants No. 2016YFA0300504, 2017YFA0302903, and 2018YFE0202600), the National Natural Science Foundation of China (NSFC) (Grants No. 11774424, 11774423, and 11822412), the Beijing Natural Science Foundation (Grant No. Z200005), the CAS Interdisciplinary Innovation Team, the Fundamental Research Funds for the Central Universities, the Research Funds of Renmin University of China (RUC) (Grant No. 18XNLG14, 19XNLG03, and 19XNLG17), and the Beijing National Laboratory for Condensed Matter Physics. N.Z. was supported by the Outstanding Innovative Talents Cultivation Funded Programs 2021 of RUC. The ARPES experiments were performed on the Dreamline beamline of SSRF and supported by MOST (2016YFA0401002), and the 03U Beamline of the SSRF is supported by ME2 project (11227902) from NSFC. Computational resources were provided by the Physical Laboratory of High Performance Computing at RUC and Shanghai Supercomputer Center.

Author contributions Z.L., K.L., H.L., and S.W. provided strategy and advice for the research. Z.L., M.L., W.S., Z.L., D.S., Y.H., and S.W. performed ARPES measurements; N.Z., and K.L. carried out DFT calculations; Q.Y., C.G., Z.T., and

H.L. synthesized the single crystals. All authors contributed to writing the manuscript.

Competing interests The authors declare no competing interests.

[1] Kuroda, K. *et al.* Evidence for magnetic Weyl fermions in a correlated metal. *Nat. Mater.* **16**, 1090–1095 (2017).

[2] Ye, L. *et al.* Massive Dirac fermions in a ferromagnetic kagome metal. *Nature* **555**, 638–642 (2018).

[3] Kim, K. *et al.* Large anomalous Hall current induced by topological nodal lines in a ferromagnetic van der waals semimetal. *Nat. Mater.* **17**, 794–799 (2018).

[4] Liu, E. *et al.* Giant anomalous Hall effect in a ferromagnetic kagome-lattice semimetal. *Nat. Phys.* **50**, 1125–1131 (2018).

[5] Wang, Q. *et al.* Large intrinsic anomalous Hall effect in half-metallic ferromagnet $\text{Co}_3\text{Sn}_2\text{S}_2$ with magnetic Weyl fermions. *Nat. Commun.* **9**, 3681 (2018).

[6] Belopolski, I. *et al.* Discovery of topological Weyl fermion lines and drumhead surface states in a room temperature magnet. *Science* **365**, 1278–1281 (2019).

[7] Liu, D. F. *et al.* Magnetic Weyl semimetal phase in a kagome crystal. *Science* **365**, 1282–1285 (2019).

[8] Morali, N. *et al.* Fermi-arc diversity on surface terminations of the magnetic Weyl semimetal $\text{Co}_3\text{Sn}_2\text{S}_2$. *Science* **365**, 1286–1291 (2019).

[9] Kang, M. *et al.* Dirac fermions and flat bands in the ideal kagome metal FeSn . *Nat. Mater.* **19**, 163–169 (2020).

[10] Lin, Z. *et al.* Dirac fermions in antiferromagnetic FeSn kagome lattices with combined space inversion and time-reversal symmetry. *Phys. Rev. B* **102**, 155103 (2020).

[11] Liu, Z. *et al.* Orbital-selective Dirac fermions and extremely flat bands in the nonmagnetic kagome metal CoSn . *Nat. Commun.* **7**, 4002 (2020).

[12] Kang, M. *et al.* Topological flat bands in frustrated kagome lattice CoSn . *Nat. Commun.* **7**, 4004 (2020).

[13] Li, M. *et al.* Dirac cone, flat band and saddle point in kagome magnet YMn_6Sn_6 . *Preprint, DOI: 10.21203/rs.3.rs-114140/v1* (2020).

[14] Lin, Z. *et al.* Flatbands and emergent ferromagnetic ordering in Fe_3Sn_2 kagome lattices. *Phys. Rev. Lett.* **121**, 096401 (2018).

[15] Yin, J.-X. *et al.* Giant and anisotropic many-body spin orbit tunability in a strongly correlated kagome magnet. *Nature* **562**, 91–95 (2018).

[16] Zhang, Y. *et al.* Emergence of Kondo lattice behavior in a van der waals itinerant ferromagnet, Fe_3GeTe_2 . *Sci. Adv.* **4** (2018).

[17] Yin, J.-X. *et al.* Negative flat band magnetism in a spin-orbit-coupled correlated kagome magnet. *Nat. Phys.* **15**, 443–448 (2019).

[18] Yin, J.-X. *et al.* Quantum-limit Chern topological magnetism in TbMn_6Sn_6 . *Nature* **583**, 533–536 (2020).

[19] Ortiz, B. R. *et al.* New kagome prototype materials: discovery of KV_3Sb_5 , RbV_3Sb_5 , and CsV_3Sb_5 . *Phys. Rev. Materials* **3**, 094407 (2019).

[20] Ortiz, B. R. *et al.* CsV_3Sb_5 : A \mathbb{Z}_2 topological kagome metal with a superconducting ground state. *Phys. Rev. Lett.* **125**, 247002 (2020).

[21] Yang, S.-Y. *et al.* Giant, unconventional anomalous Hall effect in the metallic frustrated magnet candidate, KV_3Sb_5 . *Sci. Adv.* **6**, eabb6003 (2020).

[22] Yin, Q. *et al.* Superconductivity and normal-state properties of kagome metal RbV_3Sb_5 single crystals. *Chin. Phys. Lett.* **38**, 037403 (2021).

[23] Ortiz, B. R. *et al.* Superconductivity in the \mathbb{Z}_2 kagome metal KV_3Sb_5 . *Phys. Rev. Materials* **5**, 034801 (2021).

[24] Jiang, Y.-X. *et al.* Discovery of topological charge order in kagome superconductor KV_3Sb_5 . *arXiv:2012.15709* (2021).

[25] Zhao, H. *et al.* Cascade of correlated electron states in a kagome superconductor CsV_3Sb_5 . *arXiv:2103.03118* (2021).

[26] Liang, Z. *et al.* Three-dimensional charge density wave and robust zero-bias conductance peak inside the superconducting vortex core of a kagome superconductor CsV_3Sb_5 . *arXiv:2103.04760* (2021).

[27] Chen, H. *et al.* Roton pair density wave and unconventional strong-coupling superconductivity in a topological kagome metal. *arXiv:2103.09188* (2021).

[28] Zhao, C. C. *et al.* Nodal superconductivity and superconducting domes in the topological kagome metal CsV_3Sb_5 . *arXiv:2102.08356* (2021).

[29] Chen, F. Y. *et al.* Double superconducting dome and triple enhancement of T_c in the kagome superconductor CsV_3Sb_5 under high pressure. *arXiv:2102.09328* (2021).

[30] Uykur, E., Ortiz, B. R., Wilson, S. D., Dressel, M. & Tsirlin, A. A. Optical detection of charge-density-wave instability in the non-magnetic kagome metal KV_3Sb_5 . *arXiv:2103.07912* (2021).

[31] Wang, Y. *et al.* Proximity-induced spin-triplet superconductivity and edge supercurrent in the topological kagome metal $\text{K}_{1-x}\text{V}_3\text{Sb}_5$. *arXiv:2012.05898* (2021).

[32] Li, H. X. *et al.* Observation of unconventional charge density wave without acoustic phonon anomaly in kagome superconductors AV_3Sb_5 (A = Rb, Cs). *arXiv:2012.05898* (2021).

[33] Tan, H., Liu, Y., Wang, Z. & Yan, B. Charge density waves and electronic properties of superconducting kagome metals. *arXiv:2103.06325* (2021).

[34] Feng, X., Jiang, K., Wang, Z. & Hu, J. Chiral flux phase in the kagome superconductor KV_3Sb_5 . *arXiv:2103.07097* (2021).

[35] Yu, S.-L. & Li, J.-X. Chiral superconducting phase and chiral spin-density-wave phase in a Hubbard model on the kagome lattice. *Phys. Rev. B* **85**, 144402 (2012).

[36] Wang, W.-S., Li, Z.-Z., Xiang, Y.-Y. & Wang, Q.-H. Competing electronic orders on kagome lattices at van hove filling. *Phys. Rev. B* **87**, 115135 (2013).

[37] Denner, M., Thomale, R. & Neupert, T. Analysis of charge order in the kagome metal AV_3Sb_5 (A = K, Rb, Cs). *arXiv:2103.14045* (2021).

[38] Kenney, E. M. *et al.* Absence of local moments in the kagome metal KV_3Sb_5 as determined by muon spin spectroscopy. *arXiv:2012.04737* (2021).

[39] Ni, S. *et al.* Anisotropic superconducting properties of kagome metal CsV_3Sb_5 . *arXiv:2104.00374* (2021).

[40] Duan, W. *et al.* Nodeless superconductivity in the kagome metal CsV_3Sb_5 . *arXiv:2013.11796* (2021).

[41] Zhang, Z. *et al.* Pressure-induced reemergence of superconductivity in topological kagome metal CsV_3Sb_5 . *arXiv:2103.12507* (2021).

[42] Chen, X. *et al.* Highly-robust reentrant superconductivity in CsV_3Sb_5 under pressure. *arXiv:2013.13759* (2021).

[43] Liu, Z. H. *et al.* Three dimensionality and orbital characters of the Fermi surface in $(\text{Ti}, \text{Rb})_y\text{Fe}_{2-x}\text{Se}_2$. *Phys. Rev. Lett.* **109**,

037003 (2012).

[44] Kumigashira, H. *et al.* High-resolution angle-resolved photoemission study of LaSb. *Phys. Rev. B* **58**, 7675 (1998).

[45] Norman, M. R., Lin, J. & Millis, A. J. Lifshitz transition in underdoped cuprates. *Phys. Rev. B* **81**, 180513 (2010).

[46] Liu, C. *et al.* Evidence for a Lifshitz transition in electron-doped iron arsenic superconductors at the onset of superconductivity. *Nat. Phys.* **6**, 419–423 (2010).

[47] Sunko, V. *et al.* Direct observation of a uniaxial stress–driven Lifshitz transition in Sr_2RuO_4 . *npj Quantum Mater.* **4**, 46 (2019).

[48] Chikina, A. *et al.* Turning charge–density waves into Cooper pairs. *npj Quantum Mater.* **5**, 22 (2020).

[49] Blöchl, P. E. Projector augmented-wave method. *Phys. Rev. B* **50**, 17953–17979 (1994).

[50] Kresse, G. & Joubert, D. From ultrasoft pseudopotentials to the projector augmented-wave method. *Phys. Rev. B* **59**, 1758–1775 (1999).

[51] Kresse, G. & Furthmüller, J. Efficient iterative schemes for ab initio total-energy calculations using a plane-wave basis set. *Phys. Rev. B* **54**, 11169–11186 (1996).

[52] Perdew, J. P., Burke, K. & Ernzerhof, M. Generalized gradient approximation made simple. *Phys. Rev. Lett.* **77**, 3865–3868 (1996).

[53] Grimme, S., Antony, J., Ehrlich, S. & Krieg, H. A consistent and accurate ab initio parametrization of density functional dispersion correction (DFT–D) for the 94 elements H–Pu. *J. Chem. Phys.* **132**, 154104 (2010).

[54] Wu, Q., Zhang, S., Song, H.-F., Troyer, M. & Soluyanov, A. WannierTools: An open-source software package for novel topological materials. *Comput. Phys. Commun.* **22**, 405–416 (2018).

[55] Mostofi, A. A. *et al.* An updated version of wannier90: A tool for obtaining maximally-localised Wannier functions. *Comput. Phys. Commun.* **185**, 2309–2310 (2014).